AGU100 ADVANCING EARTH AND SPACE SCIENCE

Geophysical Research Letters

RESEARCH LETTER

10.1002/2018GL076993

Magnetic Reconnection, Turbulence, and Particle Acceleration: Observations in the Earth's Magnetotail

R. E. Ergun[1,2], K. A. Goodrich[2], F. D. Wilder[2], N. Ahmadi[2], J. C. Holmes[1,2], S. Eriksson[2], J. E. Stawarz[3], R. Nakamura[4], K. J. Genestreti[4], M. Hesse[5], J. L. Burch[6], R. B. Torbert[6,7], T. D. Phan[8], S. J. Schwartz[2], J. P. Eastwood[3], R. J. Strangeway[9], O. Le Contel[10], C. T. Russell[9], M. R. Argall[7], P.-A. Lindqvist[11], L. J. Chen[12,13], P. A. Cassak[14], B. L. Giles[12], J. C. Dorelli[12], D. Gershman[14], T. W. Leonard[2], B. Lavraud[15,16], A. Retino[10], W. Matthaeus[17], and A. Vaivads[18]

[1]Department of Astrophysical and Planetary Sciences, University of Colorado Boulder, Boulder, CO, USA, [2]Laboratory of Atmospheric and Space Sciences, University of Colorado Boulder, Boulder, CO, USA, [3]The Blackett Laboratory, Imperial College London, London, UK, [4]Space Research Institute, Austrian Academy of Sciences, Graz, Austria, [5]Department of Physics and Technology, University of Bergen, Bergen, Norway, [6]Southwest Research Institute, San Antonio, TX, USA, [7]Space Science Center, University of New Hampshire, Durham, NH, USA, [8]Space Sciences Laboratory, University of California, Berkeley, CA, USA, [9]Department of Earth, Planetary, and Space Sciences, University of California, Los Angeles, CA, USA, [10]Laboratoire de Physique des Plasmas, CNRS/Ecole Polytechnique/Sorbonne Université/ Université Paris-Sud/Observatoire de Paris, Paris, France, [11]Department of Space and Plasma Physics, Royal Institute of Technology, Stockholm, Sweden, [12]NASA, Goddard Space Flight Center, Greenbelt, MD, USA, [13]Department of Astronomy, University of Maryland, College Park, MD, USA, [14]Department of Physics and Astronomy, West Virginia University, Morgantown, WV, USA, [15]Institut de Recherche en Astrophysique et Planétologie, Université de Toulouse, Toulouse, France, [16]Centre National de la Recherche Scientifique, Toulouse, France, [17]Department of Physics and Astronomy, University of Delaware, Newark, DE, USA, [18]Swedish Institute of Space Physics, Uppsala, Sweden

Key Points:

- MMS observations reveal characteristics of turbulent dissipation and particle acceleration associated with magnetic reconnection
- Perpendicular electric fields and large-amplitude parallel electric fields structures have dominant roles in turbulent dissipation
- Turbulent electric fields in a magnetic structure is shown to play a key role in accelerating electrons to greater than 100 keV energies

Correspondence to:
R. E. Ergun,
ree@lasp.colorado.edu

Citation:
Ergun, R. E., Goodrich, K. A., Wilder, F. D., Ahmadi, N., Holmes, J. C., Eriksson, S., et al. (2018). Magnetic reconnection, turbulence, and particle acceleration: Observations in the Earth's magnetotail. *Geophysical Research Letters*, *45*, 3338–3347. https://doi.org/10.1002/2018GL076993

Received 1 JAN 2018
Accepted 21 MAR 2018
Accepted article online 26 MAR 2018
Published online 19 APR 2018

Abstract We report observations of turbulent dissipation and particle acceleration from large-amplitude electric fields (***E***) associated with strong magnetic field (***B***) fluctuations in the Earth's plasma sheet. The turbulence occurs in a region of depleted density with anti-earthward flows followed by earthward flows suggesting ongoing magnetic reconnection. In the turbulent region, ions and electrons have a significant increase in energy, occasionally >100 keV, and strong variation. There are numerous occurrences of $|\mathbf{E}| > 100$ mV/m including occurrences of large potentials (>1 kV) parallel to ***B*** and occurrences with extraordinarily large $\mathbf{J} \cdot \mathbf{E}$ (***J*** is current density). In this event, we find that the perpendicular contribution of $\mathbf{J} \cdot \mathbf{E}$ with frequencies near or below the ion cyclotron frequency (f_{ci}) provide the majority net positive $\mathbf{J} \cdot \mathbf{E}$. Large-amplitude parallel ***E*** events with frequencies above f_{ci} to several times the lower hybrid frequency provide significant dissipation and can result in energetic electron acceleration.

Plain Language Summary The Magnetospheric Multiscale mission is able to examine dissipation associated with magnetic reconnection with unprecedented accuracy and frequency response. The observations show that roughly 80% of the dissipation is from the perpendicular currents and electric fields. However, large-amplitude parallel electric fields appear to play a strong role in turbulent dissipation into electrons and in electron acceleration.

1. Introduction

Magnetic reconnection in the Earth's magnetotail is understood to trigger auroral substorms (e.g., Angelopoulos et al., 2008; Nakamura et al., 2001), drive earthward flows (e.g., Angelopoulos et al., 1992; Baumjohann et al., 1989), and eject plasmoids away from Earth (Hones, 1977; Russell & McPherron, 1973). The aftermath of magnetic reconnection can leave a density-depleted plasma sheet in the Earth's midmagnetotail (15–50 R_E) with regions of intense magnetic field (***B***) fluctuations and energized ions and electrons. Magnetic reconnection may also be ongoing. In this article, we examine such a region in detail with the Magnetospheric Multiscale (MMS) mission (Burch et al., 2016) to understand the nature of turbulence associated with magnetic reconnection and the path through which ions and electrons are energized.

Plasma turbulence is active in many astrophysical settings (e.g., the interstellar medium Falceta-Gonçalves et al., 2014). It is central to the solar corona (e.g., Cranmer et al., 2015), the solar wind (e.g., Matthaeus et al., 1995), and

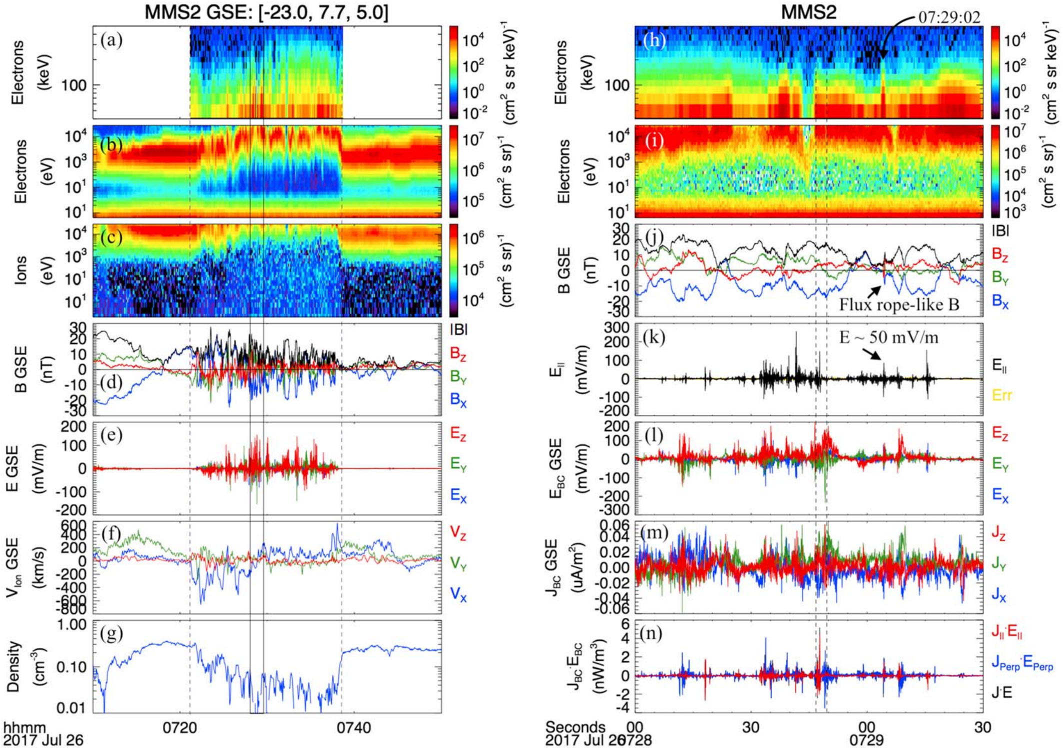

Figure 1. (left column) A 40-min overview of a strong turbulence event. (a and b) High-energy (30–500 keV) electron energy flux and low-energy (~10 eV to ~25 keV) electron differential energy flux as a function of energy averaged over all angles. (c) Ion differential energy flux (~10 eV to ~25 keV). (d) $\boldsymbol{B}$ at 16 samples/s. (e) $\boldsymbol{E}$ at 32 samples/s. (f) $\boldsymbol{V}_i$ at 5-s resolution. (g) Electron density. (right column) A magnified view of a 90-s period between the solid vertical lines on the left figure. (h and i) High-energy and low-energy electron energy fluxes from Magnetospheric Multiscale 2 (MMS2). (j) $\boldsymbol{B}$ from MMS2 at 2,048 samples/s. (k) $E_{||}$ from MMS2 at 8,192 samples/s. (l) $\boldsymbol{E}$ at the barycenter ($\boldsymbol{E}_{BC}$) at 2,048 samples/s. (m) $\boldsymbol{J}$ at the barycenter of the MMS tetrahedron at 2,048 samples/s. (n) $\boldsymbol{J}_{BC} \cdot \boldsymbol{E}_{BC}$.

active regions of the Earth's magnetosphere (Borovsky et al., 1997; Borovsky & Funsten, 2003; Chasapis et al., 2017; Stawarz et al., 2016; Stawarz, Ergun, & Goodrich, 2015; Vörös et al., 2006; Weygand et al., 2005; Zimbardo et al., 2010). In particular, plasma sheet turbulence is well established (ibid). Turbulence enables cross-scale energy transfer and influences energy exchange between electromagnetic fields and particles. One of the most important yet least understood processes of turbulence in collisionless plasmas is kinetic-scale dissipation (e.g. Karimabadi et al., 2013; TenBarge & Howes, 2013; Wan et al., 2012, 2016; Yang et al., 2017).

Turbulence is intimately associated with magnetic reconnection (e.g. Chasapis et al., 2017; Daughton et al., 2014; Eastwood et al., 2009; Ergun, Goodrich, et al., 2016; Gosling, 2007; Retinò et al., 2007; Wan et al., 2013). It appears that magnetic reconnection, particularly that which results in large-scale reconfiguration of $\boldsymbol{B}$, excites turbulence, which, in turn, drives smaller reconnection events.

MMS is designed to study magnetic reconnection, turbulence, and acceleration at high spatial and temporal resolution with four satellites in a tetrahedral formation. In this study, the average plasma density (n) is ~0.03 cm^{-3}, and ion and electron temperatures (T_i and T_e) average ~10 keV or more, so Debye lengths (λ_D) are ~4 km. The electron skin depth (λ_e) is ~30 km, whereas the MMS satellites are separated by ~15 km. Thus, MMS provides four-point, 3-D electric field ($\boldsymbol{E}$) observations within a few λ_D and accurate measurements of the current ($\boldsymbol{J}$) via the curlometer technique (Dunlop et al., 2002) due to separations less than λ_e ($\boldsymbol{J}$ is close to constant inside of the tetrahedron). Measurements of $\boldsymbol{E}$ and $\boldsymbol{J}$ support a calculation of the energy exchange between fields and particles ($\boldsymbol{J} \cdot \boldsymbol{E}$) with unprecedented frequency response and accuracy, which, in turn, enables a detailed investigation of turbulent dissipation and acceleration.

Coincident with $\boldsymbol{B}$ turbulence are large-amplitude (>100 mV/m) $\boldsymbol{E}$ fluctuations that include an equally large parallel component ($E_{||}$) and events with extraordinarily large energy exchange per particle ($\boldsymbol{J} \cdot \boldsymbol{E}/n$). The coincidence between strong ***B*** turbulence and large-amplitude turbulent ***E*** has been observed before (Ergun et al., 2009, 2015; Stawarz et al., 2015). We show that ***E*** has a central role in turbulent dissipation and particle acceleration in the plasma sheet.

2. Observations

Figure 1 (left column) displays 40 min of data that include a region of strong ***B*** turbulence in a density-depleted plasma sheet ~23 R_E from Earth. Figure 1a plots the omnidirectional electron energy fluxes from 30 to 500 keV as measured by the energetic particle detector (Mauk et al., 2016). These data are at their highest resolution (burst) and have restricted coverage in time. Immediately below (Figure 1b) is the electron differential energy fluxes from ~10 eV to ~25 keV that are measured by the fast plasma instrument (Pollock et al., 2016). Figure 1c displays the ion differential energy fluxes in the same fashion. Figure 1d displays ***B*** (Russell et al., 2016; Torbert et al., 2016) in geocentric solar equatorial (GSE) coordinates. The colors represent the directions, and the black trace is $|\boldsymbol{B}|$. Below are ***E*** (Ergun, Tucker, et al., 2016; Lindqvist et al., 2016; Torbert et al., 2016), the ion velocity ($\boldsymbol{V}_i$), and the electron density. $\boldsymbol{V}_i$ is possibly underestimated due to low density.

The vertical dashed lines demarcate a period of strong fluctuations in ***B*** (Figure 1d) and ***E*** (Figure 1e). Concurrently, electron and ion fluxes (Figures 1a–1c) show characteristic energies with significant variations. The density is depleted (Figure 1g). $\boldsymbol{V}_i$ indicates a tailward flow from ~07:22 UT (universal time) to ~07:30 UT then earthward flow afterward suggesting ongoing magnetic reconnection. Another magnetic reconnection event occurred about a half hour earlier, indicating an active magnetotail.

Figure 2 displays omnidirectional spectra of ***B*** and ***E*** averaged over the ~17.5-min period between the vertical dashed lines in Figure 1 (left column; 07:21:13 UT to 07:38:42 UT). The low-frequency ($<$ 32 Hz) ***B*** spectrum from a fluxgate magnetometer (Russell et al., 2016) is combined with the high-frequency (~8 Hz to ~4 kHz) ***B*** spectrum from a search coil magnetometer (Le Contel et al., 2016). In Figure 2, the thick orange-yellow line is the measured spectrum, whereas the blue, red, and green lines are power law fits to specific frequency ranges. The spectra do not correct for Doppler shifts nor eliminate periods in the lobes.

Turbulent systems are typically studied using wave number spectra (e.g., Kolmogorov, 1941), but only frequency spectra can be derived from time domain observations when plasma flow is varying. However, frequency spectra can provide useful information (e.g., Stawarz et al., 2016). We divide the spectra into three frequency ranges. The lowest frequency range, ~0.016 to ~0.15 Hz, lies below the average ion cyclotron frequency (f_{ci}), which is marked by a vertical dashed line in Figure 2. In this frequency range, the ***B*** spectrum shows a power law index that is consistent with an inertial cascade ($-5/3$). The ***E*** spectrum has a much shallower index (-1.08). $|\boldsymbol{E}|/|\boldsymbol{B}|$ at the lowest frequency is roughly the average Alfvén speed, so the shallow spectral index in ***E*** is consistent with dispersion of kinetic Alfvén waves.

The frequency range between f_{ci} and the average lower hybrid frequency (f_{lh}) (~8 Hz) has a steeper spectral index (-2.54) in ***B*** but a shallower spectral index in ***E*** (-0.86), which indicates further buildup of electrostatic fields. At the highest frequencies ($>$8 Hz), the ***B*** spectral index steepens to between -2.7 and -3.26, depending on the exact selection of the frequency domain for the fit. Several brief but intense bursts of whistler waves at ~100 and ~400 Hz influence the ***B*** spectral index. The ***E*** spectral index dramatically steepens at frequencies above ~3f_{lh} (~20 Hz). These observations are consistent with previously reported turbulence spectra in the magnetosphere with the exception that ***B*** has a shallower spectral index between f_{ci} and f_{lh} (Ergun et al., 2015; Stawarz et al., 2016).

Figure 1 (right column) displays 90 s of data during the time of the ion flow reversal. The period is marked in Figure 1 (left column) with solid vertical lines. Figures 1h and 1i are magnified versions of Figures 1a and 1b. ***B*** (Figure 1j) is from MMS2 at 2,048 samples/s combining the search coil and fluxgate magnetometer signals. Figure 1k is the high time resolution $E_{||}$ from MMS2, while Figure 1l plots ***E*** averaged from all spacecraft representing ***E*** at the barycenter ($\boldsymbol{E}_{BC}$).

Figure 1m displays ***J*** at the barycenter of the MMS tetrahedron ($\boldsymbol{J}_{BC}$) calculated with the curlometer technique, $(\nabla \times \boldsymbol{B})/\mu_o$ (Dunlop et al., 2002), using ***B*** signals from DC to 800 Hz. The spacecraft separations are less than λ_e so the accuracy of $\boldsymbol{J}_{BC}$ (~0.01 μA/m^2 for individual measurements) depends mostly on the accuracy

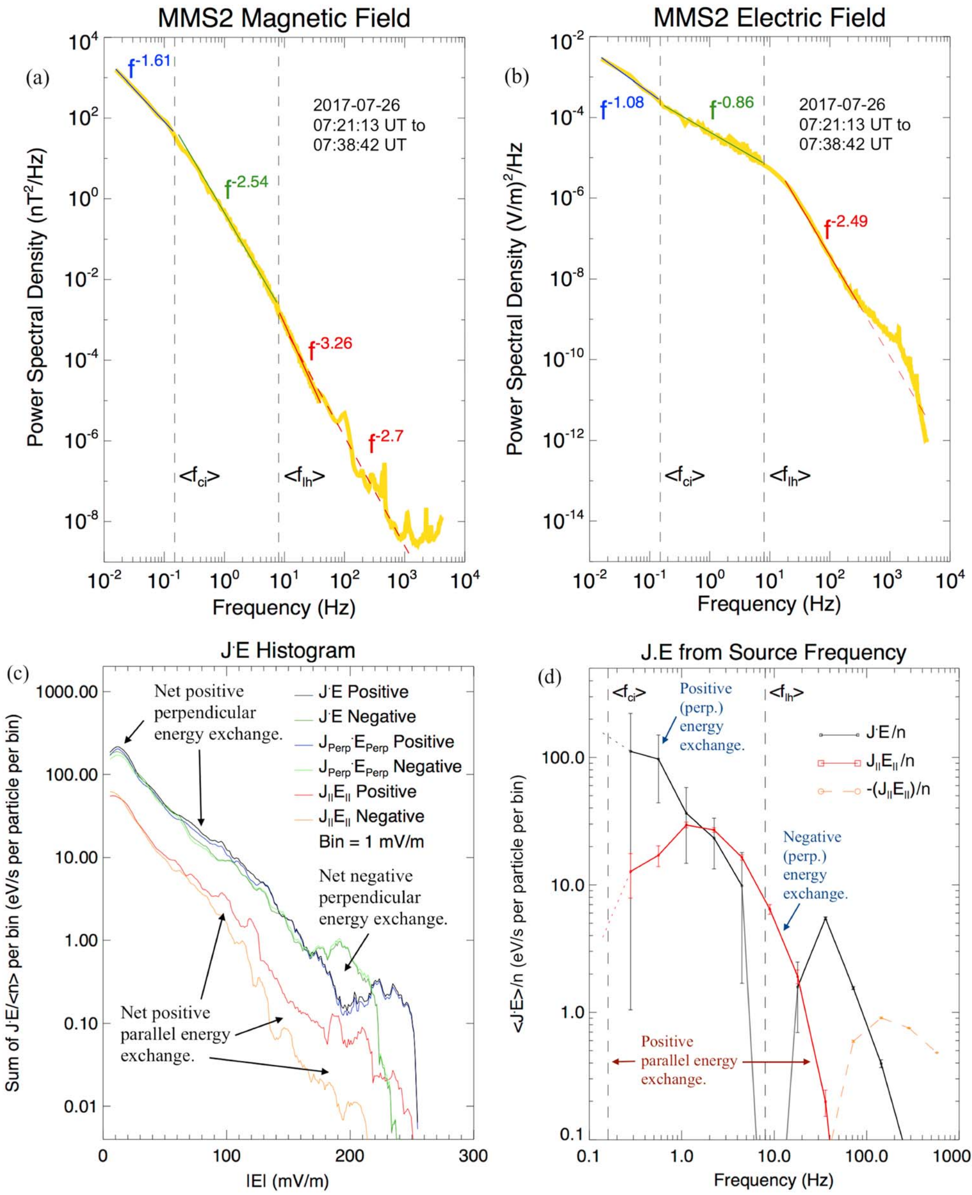

Figure 2. (a) ***B*** power spectral density (thick orange-yellow line) averaged over the ~18-min period in Figure 1 (left column). The vertical dashed lines represent the average f_{ci} and the average f_{lh}. The colored lines are power law fits to specific frequency bands. Strong, short-duration whistler emissions can be seen at ~100 Hz and ~400 Hz. (b) ***E*** power spectral density. (c) A plot of $(\boldsymbol{J}\cdot\boldsymbol{E})_{\boldsymbol{T}}/\langle n\rangle$ as a function $|\boldsymbol{E}|$ over the ~17.5-min period marked in Figure 1 (left column). The black trace is the sum of positive occurrences of $(\boldsymbol{J}\cdot\boldsymbol{E})_{\boldsymbol{T}}$, whereas the dark green trace is the sum of negative occurrences. The difference between the traces is the net energy exchange. The blue trace is the sum of positive occurrences of $(\boldsymbol{J}_\perp\cdot\boldsymbol{E}_\perp)_T$, and the light green trace is the sum of negative occurrences. The red and orange traces show the positive and negative contributions of $(J_\| E_\|)_T$. (d) The black trace is the contribution of $\langle\boldsymbol{J}\cdot\boldsymbol{E}\rangle/\langle n\rangle$ after ***J*** and ***E*** are each separated into 16 passbands. Error bars are described in the text. The red trace represents $\langle J_\| E_\|\rangle/\langle n\rangle$, which is plotted in orange dashed lines if the contribution is negative.

of ***B*** (~0.1 nT). The residual calculation, $<\nabla\cdot\boldsymbol{B}/\mu_o>_{RMS} = 3.5$ nA/m², has a nearly Gaussian distribution about 0, which supports the uncertainty of ~0.01 μA/m² (3σ) for individual measurements.

E has a DC accuracy of <2 mV/m in the spin plane components and < 4 mV/m in the axial component during this period. However, uncertainty in gain of the ***E*** signals can yield up to 5% errors. As a result, $\boldsymbol{J}_{BC}\cdot\boldsymbol{E}_{BC}$ (Figure 1n) has an accuracy of ~0.5 nW/m³ for individual measurements. Long-term averages can have

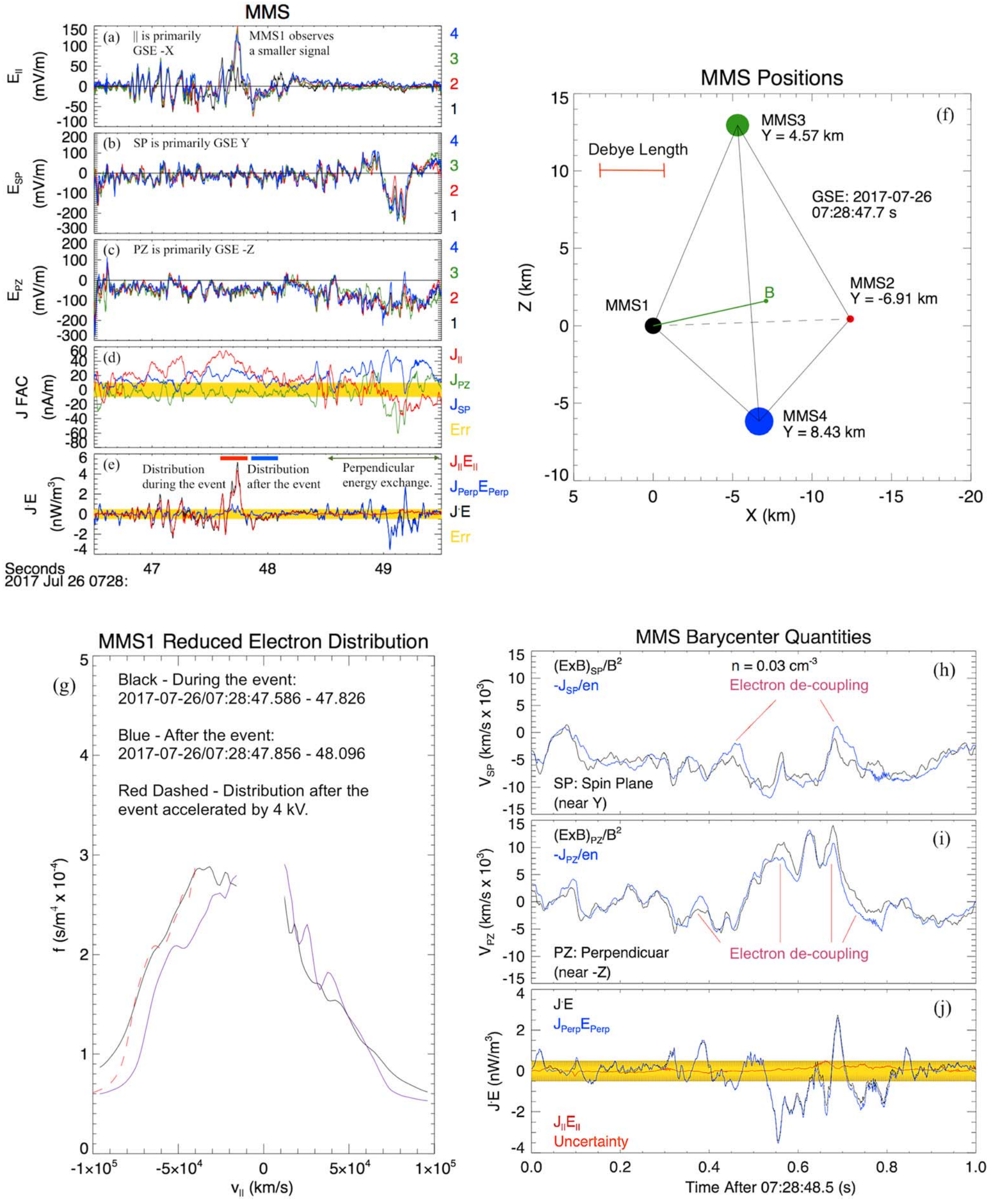

Figure 3. A 3-s view of $\boldsymbol{E}$ and $\boldsymbol{J}$. (a) $E_{||}$ at 2,048 sample/s from each of the Magnetospheric Multiscale (MMS) spacecraft. The signals are nearly identical except at ~47.7 UT. MMS1 sees a smaller signal. (b) E_{SP}, which is the perpendicular component of $\boldsymbol{E}$ in the geocentric solar equatorial (GSE) *X-Y* plane (near the spin-plane). (c) E_{PZ}, which is the perpendicular component of $\boldsymbol{E}$ near GSE $-Z$. (d) $\boldsymbol{J}$ at the barycenter of the MMS tetrahedron in field-aligned coordinates (FAC). (e) $\boldsymbol{J} \cdot \boldsymbol{E}$. (f) The MMS tetrahedron in GSE coordinates. (g) Reduced electron distributions averaged over 240 ms to increase counting statistics. The black trace is the electron distribution during the $E_{||}$ event as marked in panel e. The blue trace is the electron distribution after the event. The dashed red trace is the electron distribution after the event accelerated by 4 kV. (h) The perpendicular V_e in the *SP* direction calculated from $\boldsymbol{E} \times \boldsymbol{B}/B^2$ (black trace) and $\boldsymbol{V}_e - \boldsymbol{V}_i$ calculated from $-J_{SP}/en$ (blue trace). (i) V_e in the *PZ* direction calculated in the same fashion as in panel h. (j) $\boldsymbol{J} \cdot \boldsymbol{E}$. The orange/yellow region represents the uncertainty of individual measurements.

higher accuracy if DC baselines are removed. $\boldsymbol{J}_{BC} \cdot \boldsymbol{E}_{BC}$ (Figure 1m) is plotted in black with the perpendicular contribution in blue and the parallel contribution in red.

Figure 3 shows a 3-s view of an event with large $\boldsymbol{J}_{BC} \cdot \boldsymbol{E}_{BC}$ (which we shorten to $\boldsymbol{J} \cdot \boldsymbol{E}$ from here on). The period is marked in Figure 1 (right column) with dashed vertical lines. Figures 3a–3c display $\boldsymbol{E}$ from each of the four MMS spacecraft in field-aligned coordinates (FAC). Figure 3a plots $E_{||}$ with the colors representing the spacecraft. Since $\langle \boldsymbol{B} \rangle = [-14.2, 3.1, 3.5]$ nT during the 3-s period, $E_{||}$ is primarily in GSE $-X$. E_{SP} (Figure 3b) is a perpendicular component that lies in the GSE *X*-*Y* plane ("SP" stands for "spin plane") and is primarily in GSE $+Y$. E_{PZ} (Figure 3c) is the perpendicular component that lies closest to GSE $-Z$. Figure 3d plots $\boldsymbol{J}_{BC}$ in the same FAC system, and Figure 3e plots $\boldsymbol{J}\cdot\boldsymbol{E}$.

One noticeable feature in Figures 3a–3c is that $\boldsymbol{E}$ from the four spacecraft are nearly identical. However, the large-amplitude $E_{||}$ structure at 07:28:47.7 UT differs in MMS1, which indicates a change on Debye scales. Because MMS1 observes a smaller signal, the velocity of the $E_{||}$ structure is difficult to determine by time delay analysis between spacecraft. Three-spacecraft time delays indicate a $-SP$ $(-Y)$ component. Furthermore, $\boldsymbol{E}\times\boldsymbol{B}/B^2$ is roughly 4,000 km/s in $-SP$ $(-Y)$ and $-J_{SP}/en$ (see Figure 3d; $n \sim 0.03$ cm^{-3}) indicates the same speed in $-SP$ $(-Y)$, so if the structure is embedded in the perpendicular electron flow, it may have a large speed perpendicular to $\boldsymbol{B}$. There are no measureable probe-to-probe delays on individual spacecraft, which indicates a structure speed greater than 2,500 km/s. Moreover, the spacecraft positions (Figure 3f) are such that perpendicular travel is needed if an $E_{||}$ structure partly misses the MMS1 spacecraft.

Figure 3g displays electron distributions measured by MMS1 during (black trace) and after (blue trace) the $E_{||}$ event. MMS1 is positioned in the $-\boldsymbol{B}$ $(+X)$ direction (Figure 3f) so electrons should be accelerated toward MMS1. The MMS1 electron distribution during the $E_{||}$ event (black trace) is consistent with ~4 kV increase (dashed red trace) of the electron distribution immediately after the $E_{||}$ event (blue trace). This ~4 kV increase suggests a 4 kV potential structure at the location of MMS2, MMS3, and MMS4. Given a 4 kV potential and $< E_{||} > \sim 100$ mV/m, the $E_{||}$ structure should extend roughly 40 km along $\boldsymbol{B}$ (~13 λ_D). It appears to be embedded in the electron plasma traveling perpendicular to $\boldsymbol{B}$. Its speed along $\boldsymbol{B}$ is not determined.

Concurrent with the large-amplitude $E_{||}$ signal (Figure 3a) is a large, positive excursion in $\boldsymbol{J}\cdot\boldsymbol{E}$ (Figure 3e). If there is no flow, $\boldsymbol{J}\cdot\boldsymbol{E}\,\delta t/n$ (δt ~0.1 s) implies energization of 60 keV per particle, which is extraordinarily large. However, the parallel electron velocity ($-J_{||}/en$ = ~8,000 km/s along $-\boldsymbol{B}$ or in the $+X$ direction) indicates that the energy could be shared by up to 20 times ($J_{||}/en\,\delta t/L$, L~40 km) the number of particles as in the no-flow case. Considering all factors, the data are consistent with a ~4 kV double-layer-like structure (e.g., Ergun et al., 2009; Newman et al., 2001) that supports strong, positive $\boldsymbol{J}\cdot\boldsymbol{E}$.

Figure 3 also provides insight into the perpendicular energy exchange process. Starting at ~07:28:49 UT, there is a large negative $\boldsymbol{J}_\perp\cdot\boldsymbol{E}_\perp$ (Figure 3e) as E_{SP} reaches -250 mV/m (Figure 3b). Figures 3h and 3i plot two components of the estimated electron velocity ($\boldsymbol{V}_e$) derived via two methods. The black trace is $\boldsymbol{E}\times\boldsymbol{B}/B^2$, and the blue trace is $-\boldsymbol{J}_{BC}/en$, which is $\boldsymbol{V}_e - \boldsymbol{V}_i$. n is set at 0.03 cm^{-3} during the period, which gives the best agreement (median of difference is 0) between the two signals. In Figure 2, $\boldsymbol{E}\times\boldsymbol{B}/B^2$ and $-\boldsymbol{J}_{BC}/en$ systematically differ when $\boldsymbol{J}_\perp\cdot\boldsymbol{E}_\perp \neq 0$.

The electron fluid equation can be written as

$$\boldsymbol{E}+\boldsymbol{V}_e\times\boldsymbol{B} = -\frac{m_e}{e}\frac{\partial \boldsymbol{V}_e}{\partial t} - \frac{(\boldsymbol{V}_e\cdot\nabla)\boldsymbol{V}_e}{e} - \frac{\nabla\cdot\boldsymbol{P_e}}{en} \tag{1}$$

where $\boldsymbol{P}_e$ is the pressure tensor and m_e is the electron mass. If $\boldsymbol{V}_i \ll \boldsymbol{V}_e$, then $\boldsymbol{E}\times\boldsymbol{B}/B^2$ and $-\boldsymbol{J}_{BC}/en$ must differ when $\boldsymbol{J}_\perp\cdot\boldsymbol{E}_\perp \neq 0$ since $(\boldsymbol{E}\times\boldsymbol{B})\cdot\boldsymbol{E} = 0$. $\boldsymbol{V}_i$ cannot account for the majority of energy exchange in this event because $\boldsymbol{E}\times\boldsymbol{B}/B^2$ and $-\boldsymbol{J}_{BC}/en$ differ by up to ~5,000 km/s, which exceeds possible ion flows. Density variations may make $-\boldsymbol{J}_{BC}/en$ an inaccurate representation of $\boldsymbol{V}_e$, but could not account for the systematic nature of the differences between $\boldsymbol{E}\times\boldsymbol{B}/B^2$ and $-\boldsymbol{J}_{\mathrm{BC}}/en$ when $\boldsymbol{J}_\perp\cdot\boldsymbol{E}_\perp \neq 0$. These results imply that electrons are "de-coupling" from $\boldsymbol{B}$; that is, $\boldsymbol{E}+\boldsymbol{V}_e\times\boldsymbol{B} \neq 0$ during occurrences of $\boldsymbol{J}_\perp\cdot\boldsymbol{E}_\perp \neq 0$ indicating a divergence in $\boldsymbol{P}_e$ or convective acceleration.

Importantly, there are several occasions of concurrent increases in energetic electron fluxes during large-amplitude $\boldsymbol{E}$ events and large $\boldsymbol{J}\cdot\boldsymbol{E}$ events. For example (Figure 1, right column, at 07:29:02 UT—see arrow in panel h), $\langle \boldsymbol{J}\cdot\boldsymbol{E}\,\rangle\delta t/n$ = 19 keV per particle (Figure 1n) in a flux rope-like structure (see arrow in Figure 1j), and, simultaneously, electron energy fluxes are seen over 100 keV (Figure 1h). It appears that acceleration by turbulent $\boldsymbol{E}$ can contribute to electron acceleration to over 100 keV.

3. Analysis

A case-by-case examination of the large $\boldsymbol{J}\cdot\boldsymbol{E}$ events (which includes ~20 events) reveals a pattern in which $J_{||}E_{||}$ appears to have a positive bias, while $\boldsymbol{J}_\perp\cdot\boldsymbol{E}_\perp$ has equal positive and negative events. It is clear that that

$J_{\|}E_{\|}$ and $\boldsymbol{J}_{\perp} \cdot \boldsymbol{E}_{\perp}$ are distinct physical processes. One may also (incorrectly) come to the conclusions that $J_{\|}E_{\|}$ provides most of the turbulent dissipation (assuming that it is irreversible) whereas $\boldsymbol{J}_{\perp} \cdot \boldsymbol{E}_{\perp}$ appears to be consistent with reversible energy exchange.

A deeper investigation reveals some interesting characteristics of $\boldsymbol{J} \cdot \boldsymbol{E}$. We examine long-term intervals by removing the baseline, $\langle \boldsymbol{J} \rangle \cdot \langle \boldsymbol{E} \rangle$. In addition, a small offset in J_y (GSE) is removed. We label turbulent energy exchange as

$$(\boldsymbol{J} \cdot \boldsymbol{E})_T = \boldsymbol{J} \cdot \boldsymbol{E} - \langle \boldsymbol{J} \rangle \cdot \langle \boldsymbol{E} \rangle \tag{2}$$

Averaged over the entire turbulent interval $\langle \boldsymbol{J} \cdot \boldsymbol{E} \rangle_T / \langle n \rangle = \sim 500$ eV/s per particle, ~80% of which is from $\langle \boldsymbol{J}_{\perp} \cdot \boldsymbol{E}_{\perp} \rangle_T / \langle n \rangle$ (~400 eV/s per particle) and ~20% of which is from $\langle J_{\|}E_{\|} \rangle_T / \langle n \rangle$ (~100 eV/s per particle). These values have high uncertainty (~33%). This result appears to contradict the case-by-case examination of large-amplitude events. Furthermore, we observe $\langle E_y \rangle = 2.8 \pm 0.5$ mV/m, so if we estimate $\langle J_y \rangle$ to be ~ 1 nA/m^3 (well below measurement accuracy) using a ~2 R_E thick plasma sheet (B_x changes 30 nT in 2 R_E), then $\langle \boldsymbol{J} \rangle \cdot \langle \boldsymbol{E} \rangle / \langle n \rangle$ could be over 1,000 eV/s per particle.

Figure 2c plots $(\boldsymbol{J} \cdot \boldsymbol{E})_T$ as a function $|\boldsymbol{E}|$ over the entire turbulent interval and normalized by $\langle n \rangle$. The bin size is 1 mV/m, and the results are smoothed over nine bins. The traces are $(\sum (\boldsymbol{J} \cdot \boldsymbol{E})_T) / \langle n \rangle N$, where N is the number of samples (2,048 samples/s). The black trace is the sum of samples with $(\boldsymbol{J} \cdot \boldsymbol{E})_T > 0$, and the dark green trace includes samples with $(\boldsymbol{J} \cdot \boldsymbol{E})_T < 0$. The difference (not displayed) is the net energy exchange. The blue and light green traces are, respectively, positive and negative contributions of $(\boldsymbol{J}_{\perp} \cdot \boldsymbol{E}_{\perp})_T$. The red and orange traces show positive and negative contributions from $(J_{\|}E_{\|})_T$. Energy exchange is clearly dominated by $(\boldsymbol{J}_{\perp} \cdot \boldsymbol{E}_{\perp})_T$.

In Figure 2c, there is a significant net positive energy exchange in $(\boldsymbol{J}_{\perp} \cdot \boldsymbol{E}_{\perp})_T$ when $|\boldsymbol{E}| < 150$ mV/m (Figure 2c is a logarithmic plot so the difference at $|\boldsymbol{E}| \sim 80$ mV/m dominates), while at larger $\boldsymbol{E}$, $(J_{\|}E_{\|})_T$ is systematically positive, which is consistent with the case-by-case examination. There are both net negative and net positive $(\boldsymbol{J}_{\perp} \cdot \boldsymbol{E}_{\perp})_T$ when $|\boldsymbol{E}| > 150$ mV/m, which, again, is consistent with the case-by-case examination.

Taking the investigation one step further, $\boldsymbol{J} \cdot \boldsymbol{E}$ is separated into frequency bins (Figure 2d). Here baselines do not need to be removed. Since $\boldsymbol{J} \cdot \boldsymbol{E}$ is a product, the source terms, $\boldsymbol{J}_{BC}$ and $\boldsymbol{E}_{BC}$, are each filtered into 16 passbands with center frequencies separated by a factor of 2 (see Cully et al., 2008; Ergun, Tucker, et al., 2016 for details on passband filters). The filtering is performed in FAC so that the parallel and perpendicular components are not mixed. Figure 2d plots the net contribution $\langle \boldsymbol{J} \cdot \boldsymbol{E} \rangle / \langle n \rangle$ in each of the passbands. The black trace is $\langle \boldsymbol{J} \cdot \boldsymbol{E} \rangle / \langle n \rangle$. There is one negative value at 9 Hz which is not shown. The red solid line and squares represent $\langle J_{\|}E_{\|} \rangle / \langle n \rangle$, which is plotted with dashed orange lines and circles when its value is negative. $\langle \boldsymbol{J}_{\perp} \cdot \boldsymbol{E}_{\perp} \rangle / \langle n \rangle$ can be deduced by subtracting $\langle J_{\|}E_{\|} \rangle / \langle n \rangle$ from $\langle \boldsymbol{J} \cdot \boldsymbol{E} \rangle / \langle n \rangle$. Values of $\langle J_{\|}E_{\|} \rangle / \langle n \rangle$ are not valid at the lowest frequencies since calibration routines employ $\boldsymbol{E} \cdot \boldsymbol{B} = 0$ over long periods to determine baseline offsets. Values of $\langle \boldsymbol{J} \cdot \boldsymbol{E} \rangle / \langle n \rangle$ are also questionable at frequencies less than f_{ci} since there is no mathematical basis for separating the two perpendicular components in a strongly fluctuating $\boldsymbol{B}$ prior to applying the passband filters.

The error bars in Figure 2d are derived by applying several methods of performing the band-pass filtering. In addition to taking the product of the passbands, the product of $\boldsymbol{E}_{BC}$ (passbands) with $\boldsymbol{J}_{BC}$ (unfiltered) and the product of $\boldsymbol{E}_{BC}$ (unfiltered) with $\boldsymbol{J}_{BC}$ (passbands) are calculated. $\langle \boldsymbol{J} \cdot \boldsymbol{E} \rangle / \langle n \rangle$ is also derived from GSE signals. To test the sensitivity to the strongly varying $\boldsymbol{B}$, baseline offsets in all components of $\boldsymbol{E}_{BC}$ with $\boldsymbol{J}_{BC}$ are introduced, and the products are recalculated. The error bars (Figure 2d) represent the standard deviation of ~75 different calculations.

This exercise demonstrates that the passband calculations are meaningful for frequencies greater than f_{ci}, but standard deviations exceed the mean values if frequencies are less than f_{ci}. Strong fluctuations in $\boldsymbol{B}$ with frequencies less than f_{ci} apparently prohibit calculation of $\boldsymbol{J} \cdot \boldsymbol{E}$.

A significant feature in Figure 2d is the positive passband contributions of $\langle J_{\|}E_{\|} \rangle / \langle n \rangle$ with frequencies between f_{ci} and several times f_{lh}. This frequency range has the steepened spectral index of $\boldsymbol{B}$ (Figure 2a) and a shallow spectral index in $\boldsymbol{E}$ (Figure 2b), which indicates a buildup of electrostatic $\boldsymbol{E}$. Positive $\boldsymbol{J} \cdot \boldsymbol{E}$. at the frequencies near f_{lh} appears to be dominated by $J_{\|}E_{\|}$. Furthermore, the case-by-case examination and Figure 2c suggest that $J_{\|}E_{\|}$ is dominated by large-amplitude, nonlinear $E_{\|}$ structures and that $J_{\|}E_{\|}$ mainly acts on electrons.

Interestingly, a sum of the passband contributions of $\langle J_{\|}E_{\|}\rangle/\langle n\rangle$ above f_{ci} is ~120 eV/s per particle, which is in agreement $\langle J_{\|}E_{\|}\rangle_T/\langle n\rangle$.

Another interesting feature in Figure 2d is that the positive $\boldsymbol{J}\cdot\boldsymbol{E}$ in the frequency range just above f_{ci} is dominated by $\boldsymbol{J}_\perp\cdot\boldsymbol{E}_\perp$ (Figure 2d), which may involve energy input into ions as well as electrons. Summing the passband components of $\langle\boldsymbol{J}\cdot\boldsymbol{E}\rangle/\langle n\rangle$ at frequencies greater that f_{ci} yields a net contribution of ~250 eV/s per particle, which is roughly one half of the net of $\langle\boldsymbol{J}\cdot\boldsymbol{E}\rangle_T/\langle n\rangle$ = ~500 eV/s per particle. Thus, there may be a significant contribution of $\boldsymbol{J}\cdot\boldsymbol{E}$ at frequencies at or below f_{ci}, primarily from $\boldsymbol{J}_\perp\cdot\boldsymbol{E}_\perp$.

It is difficult to determine if a net positive $\boldsymbol{J}\cdot\boldsymbol{E}$ is received by ions or by electrons. The case-by-case analysis of the largest $\boldsymbol{J}\cdot\boldsymbol{E}$ events suggests that electrons are the recipient of most of the net positive energy from turbulence, $\langle\boldsymbol{J}\cdot\boldsymbol{E}\rangle_T$. However, since $\langle\boldsymbol{J}_\perp\cdot\boldsymbol{E}_\perp\rangle_T$ carries roughly 80% of the positive energy exchange and it acts at frequencies near and possibly below f_{ci}, ions may be the recipient of some of the turbulent energy. To complicate matters, it is likely that the ions are the main recipient of the baseline energy exchange ($\langle\boldsymbol{J}\rangle\cdot\langle\boldsymbol{E}\rangle$) since they are not gyrotropic (e.g., Speiser, 1965).

As a crude test, we examine ion and electron observations (Figure 1). T_i rises from ~5 keV outside of the turbulent region to >20 keV in turbulent region (Figure 1c). Since $\langle\boldsymbol{J}\rangle\cdot\langle\boldsymbol{E}\rangle/\langle n\rangle$ is on the order of ~1,000 eV/s per ion (assuming ions are the recipients of the energy), the baseline is sufficient to energize ions to 20 keV in 15 s. Assuming that ions dwell in the turbulent region on 15-s time scales, this energization rate can sustain the observed T_i.

On the other hand, electrons are likely energized by the higher-frequency fields. As a minimum, the total of $\langle J_{\|}E_{\|}\rangle/\langle n\rangle$ between f_{ci} and several times f_{lh} is ~120 eV/s per electron (Figure 2d), which is sufficient to account for T_e increasing from ~1 keV outside of the turbulent region to >5 keV in turbulent region in less than 1 min. The perpendicular contribution speeds the heating process. As in the case with ions, the energization rate of the electrons appears to be sufficient to sustain the observed T_e in the turbulent region. Electron and ion heating strongly supports the fact that that the net positive energy exchange in $\boldsymbol{J}\cdot\boldsymbol{E}$ is irreversible (dissipation).

4. Conclusions

We examined an ~17.5-min period of strong turbulence in a depleted plasma sheet, which presumably started during an earlier magnetic reconnection event. Magnetic reconnection appears to be ongoing. The values of λ_D (~4 km) and λ_e (~30 km) with respect the MMS tetrahedron spacing (~15 km) allow for an unprecedented view into turbulent dissipation. The close spacing with respect to λ_e makes the curlometer technique (Dunlop et al., 2002) exceptionally accurate. The close spacing of a few λ_D yields good coherence between $\boldsymbol{E}$ from the four spacecraft, so $\boldsymbol{J}\cdot\boldsymbol{E}$ is remarkably accurate.

A case-by-case examination of large-amplitude events shows that $\boldsymbol{J}_\perp\cdot\boldsymbol{E}_\perp$ and $J_{\|}E_{\|}$ have quite different behavior. $J_{\|}E_{\|}$ often has a positive bias, albeit with many events having negative $J_{\|}E_{\|}$. The net $J_{\|}E_{\|}$ contribution is largely from large-amplitude $E_{\|}$ events in the form of nonlinear structures such as double layers. To the contrary, large-amplitude $\boldsymbol{J}_\perp\cdot\boldsymbol{E}_\perp$events appeared to have a slightly negative bias, if any. A close examination of the events with $\boldsymbol{J}_\perp\cdot\boldsymbol{E}_\perp \neq 0$ showed that the electrons must partially decouple from $\boldsymbol{B}$, implying a divergence in the electron stress tensor.

Evidence of electron acceleration to >100 keV energies is presented. One of the most convincing events has $\boldsymbol{E}$ fluctuations >50 mV/m including $E_{\|}$ embedded in flux rope-like $\boldsymbol{B}$ structure, with $\langle\boldsymbol{J}\cdot\boldsymbol{E}\rangle\delta t \sim$ 19 keV/particle, which is extraordinarily large. This event provides persuasive evidence that turbulent $\boldsymbol{E}$ can directly energize electrons to >100 keV energies. This evidence supports the fact that that turbulence from reconnection can lead to strong particle acceleration, particularly from $E_{\|}$ (Egedal et al., 2012).

A statistical analysis of $\boldsymbol{J}\cdot\boldsymbol{E}$ (Figure 2c) reveals that turbulent energy exchange appears to be dominated by $\boldsymbol{J}_\perp\cdot\boldsymbol{E}_\perp$, a characteristic that was not apparent in the case-by-case examination of large-amplitude events. The net positive $\boldsymbol{J}_\perp\cdot\boldsymbol{E}_\perp$ is in a large number of moderate amplitude (10–150 mV/m) $\boldsymbol{E}$ occurrences, whereas the large-amplitude occurrences of $\boldsymbol{J}_\perp\cdot\boldsymbol{E}_\perp$ have little net contribution. With $\boldsymbol{E}$ above ~50 mV/m, $J_{\|}$ $E_{\|}$ has a clear net positive bias, which is consistent with turbulent dissipation. Over the entire interval, roughly 80% of the dissipation comes from $\boldsymbol{J}_\perp\cdot\boldsymbol{E}_\perp$and 20% comes from $J_{\|}E_{\|}$.

$\boldsymbol{J} \cdot \boldsymbol{E}$, when separated into passbands (Figure 2d), reveals that the contribution to turbulent dissipation from $\boldsymbol{J}_\perp \cdot \boldsymbol{E}_\perp$ is positive in the frequency band just above f_{ci}. A significant positive contribution $\boldsymbol{J}_\perp \cdot \boldsymbol{E}_\perp$, may lie at or just below f_{ci}. Large-amplitude, small-scale $\boldsymbol{J}_\perp \cdot \boldsymbol{E}_\perp$ events are shown to act on electrons. Turbulent dissipation from $J_\| E_\|$ dominates a frequency band that ranges from a few times f_{ci} to several times f_{lh} and acts primarily on electrons.

In summary, MMS observations have revealed characteristics of turbulent dissipation and particle acceleration associated with magnetic reconnection. $\boldsymbol{E}_\perp$ and large-amplitude, nonlinear $E_{||}$ structures have distinct but dominant roles in turbulent dissipation. Turbulent $\boldsymbol{E}$ including significant $E_{||}$ in a magnetic structure is clearly demonstrated to play a central role in accelerating electrons to greater than 100 keV energies.

Acknowledgments
This work was funded by the NASA MMS project. The SCM instruments on MMS are supported by CNES, CNRS-INSIS, and CNRS-INSU. The data are available from the MMS Science Data Center (https://lasp.colorado.edu/mms/sdc/public/). The authors recognize the tremendous effort in developing and operating the MMS spacecraft and instruments and sincerely thank all involved.

References

Angelopoulos, V., Baumjohann, W., Kennel, C. F., Coroniti, F. V., Kivelson, M. G., Pellat, R., et al. (1992). Bursty bulk flows in the inner central plasma sheet. *Journal of Geophysical Research*, *97*(A4), 4027–4039. https://doi.org/10.1029/91JA02701

Angelopoulos, V., McFadden, J. P., Larson, D., Carlson, C. W., Mende, S. B., Frey, H., et al. (2008). Tail reconnection triggering substorm onset. *Science*, *321*(5891), 931–935. https://doi.org/10.1126/science.1160495

Baumjohann, W., Paschmann, G., & Cattell, C. A. (1989). Average plasma properties in the central plasma sheet. *Journal of Geophysical Research*, *94*(A6), 6597–6606. https://doi.org/10.1029/JA094iA06p06597

Borovsky, J. E., Elphic, R. C., Funsten, H. O., & Thomsen, M. F. (1997). The Earth's plasma sheet as a laboratory for flow turbulence in high-β MHD. *Journal of Plasma Physics*, *57*(1), 1–34. https://doi.org/10.1017/S0022377896005259

Borovsky, J. E., & Funsten, H. O. (2003). MHD turbulence in the Earth's plasma sheet: Dynamics, dissipation, and driving. *Journal of Geophysical Research*, *108*(A7), 1284. https://doi.org/10.1029/2002JA009625

Burch, J. L., Moore, T. E., Torbert, R. B., & Giles, B. L. (2016). Magnetospheric Multiscale overview and science objectives. *Space Science Reviews*, *199*(1-4), 5–21. https://doi.org/10.1007/s11214-015-0164-9

Chasapis, A., Matthaeus, W. H., Parashar, T. N., Le Contel, O., Retinò, A., Breuillard, H., et al. (2017). Electron heating at kinetic scales in magnetosheath turbulence. *Astrophysical Journal*, *836*(2). https://doi.org/10.3847/1538-4357/836/2/247

Cranmer, S. R., Asgari-Targhi, M., Miralles, M. P., Raymond, J. C., Strachan, L., Tian, H., & Woolsey, L. N. (2015). The role of turbulence in coronal heating and solar wind expansion. *Philosophical Transactions of the Royal Society A*, *373*(2041), 20140148. https://doi.org/10.1098/rsta.2014.0148

Cully, C. M., Ergun, R. E., Stevens, K., Nammari, A., & Westfall, J. (2008). The THEMIS Digital Fields Board. *Space Science Reviews*, *141*(1-4), 343–355. https://doi.org/10.1007/s11214-008-9417-1

Daughton, W., Nakamura, T. K. M., Karimabadi, H., Roytershteyn, V., & Loring, B. (2014). Computing the reconnection rate in turbulent kinetic layers by using electron mixing to identify topology. *Physics of Plasmas*, *21*(5), 52307. https://doi.org/10.1063/1.4875730

Dunlop, M. W., Balogh, A., Glassmeier, K.-H., & Robert, P. (2002). Four-point cluster application of magnetic field analysis tools: The curlometer. *Journal of Geophysical Research*, *107*(A11), 1384. https://doi.org/10.1029/2001JA005088

Eastwood, J. P., Phan, T. D., Bale, S. D., & Tjulin, A. (2009). Observations of turbulence generated by magnetic reconnection. *Physical Review Letters*, *102*(3), 035001. https://doi.org/10.1103/PhysRevLett.102.035001

Egedal, J., Daughton, W., & Le, A. (2012). Large-scale electron acceleration by parallel electric fields during magnetic reconnection. *Nature Physics*, *8*, 321–324. https://doi.org/10.1038/nphys2249

Ergun, R. E., Andersson, L., Tao, J., Angelopoulos, V., Bonnell, J., McFadden, J. P., et al. (2009). Observations of double layers in Earth's plasma sheet. *Physical Review Letters*, *102*(15), 155002. https://doi.org/10.1103/PhysRevLett.102.155002

Ergun, R. E., Goodrich, K. A., Stawarz, J. E., Andersson, L., & Angelopoulos, V. (2015). Large-amplitude electric fields associated with bursty bulk flow braking in the Earth's plasma sheet. *Journal of Geophysical Research: Space Physics*, *120*, 1832–1844. https://doi.org/10.1002/2014JA020165

Ergun, R. E., Goodrich, K. A., Wilder, F. D., Holmes, J. C., Stawarz, J. E., Eriksson, S., et al. (2016). Magnetospheric Multiscale satellites observations of parallel electric fields associated with magnetic reconnection. *Physical Review Letters*, *116*(23), 235102. https://doi.org/10.1103/PhysRevLett.116.235102

Ergun, R. E., Tucker, S., Westfall, J., Goodrich, K. A., Malaspina, D. M., Summers, D., et al. (2016). The axial double probe and fields signal processing for the MMS mission. *Space Science Reviews*, *199*, 67–188. https://doi.org/10.1007/s11214-014-0115

Falceta-Gonçalves, D., Kowal, G., Falgarone, E., & Chian, A. C.-L. (2014). Turbulence in the interstellar medium. *Nonlinear Processes in Geophysics*, *21*(3), 587–604. https://doi.org/10.5194/npg-21-587-2014

Gosling, J. T. (2007). Observations of magnetic reconnection in the turbulent high-speed solar wind. *The Astrophysical Journal*, *671*(1), L73–L76. https://doi.org/10.1086/524842

Hones, E. W. Jr. (1977). Substorm processes in the magnetotail: Comments on 'On hot tenuous plasmas, fireballs, and boundary layers in the Earth's magnetotail' by L. A. Frank, K. L. Ackerson, and R. P. Lepping. *Journal of Geophysical Research*, *82*(35), 5633–5640. https://doi.org/10.1029/JA082i035p05633

Karimabadi, H., Roytershteyn, V., Wan, M., Matthaeus, W. H., Daughton, W., Wu, P., et al. (2013). Coherent structures, intermittent turbulence, and dissipation in high-temperature plasmas. *Physics of Plasmas*, *20*(1), 12303. https://doi.org/10.1063/1.4773205

Kolmogorov, A. N. (1941). Dissipation of energy in locally isotropic turbulence. In *Doklady Akademiia Nauk SSSR* (Vol. 32, 16 pp.) (reprinted in Proc. R. Soc. A, 434, 15–17, 1990).

Le Contel, O., Leroy, P., Roux, A., Coillot, C., Alison, D., Bouabdellah, A., et al. (2016). The search-coil magnetometer for MMS. *Space Science Reviews*, *199*(1-4), 257–282. https://doi.org/10.1007/s11214-014-0096-9

Lindqvist, P.-A., Olsson, G., Torbert, R. B., King, B., Granoff, M., Rau, D., et al. (2016). The spin-plane double probe instrument for MMS. *Space Science Reviews*, *199*(1-4), 137–165. https://doi.org/10.1007/s11214-014-0116-9

Matthaeus, W. H., Bieber, J. W., & Zank, G. P. (1995). Unquiet on any front: Anisotropic turbulence in the solar wind. *Reviews of Geophysics*, *33*, 609–614. https://doi.org/10.1029/95RG00496

Mauk, B. H., Blake, J. B., Baker, D. N., Clemmons, J. H., Reeves, G. D., Spence, H. E., et al. (2016). The Energetic Particle Detector (EPD) investigation and the Energetic Ion Spectrometer (EIS) for the Magnetospheric Multiscale (MMS) mission. *Space Science Reviews*, *199*(1-4), 471–514. https://doi.org/10.1007/s11214-014-0055-5

Nakamura, R., Baumjohann, W., Brittnacher, M., Sergeev, V. A., Kubyshkina, M., Mukai, T., & Liou, K. (2001). Flow bursts and auroral activations: Onset timing and foot point location. *Journal of Geophysical Research*, *106*(A6), 10,777–10,789. https://doi.org/10.1029/2000JA000249

Newman, D. L., Goldman, M. V., Ergun, R. E., & Mangeney, A. (2001). Formation of double layers and electron holes in a current-driven space plasma. *Physical Review Letters*, *87*(25), 255001. https://doi.org/10.1103/PhysRevLett.87.255001

Pollock, C., Moore, T., Jacques, A., Burch, J., Gliese, U., Saito, Y., et al. (2016). Fast plasma investigation for Magnetospheric Multiscale. *Space Science Reviews*, *199*, 331–406. https://doi.org/10.1007/s11214-016-0245-4

Retinò, A., Sundkvist, D., Vaivads, A., Mozer, F., André, M., & Owen, C. J. (2007). In situ evidence of magnetic reconnection in turbulent plasma. *Nature Physics*, *3*(4), 235–238. https://doi.org/10.1038/nphys574

Russell, C. T., Anderson, B. J., Baumjohann, W., Bromund, K. R., Dearborn, D., Fischer, D., et al. (2016). The Magnetospheric Multiscale Magnetometers. *Space Science Reviews*, *199*(1-4), 189–256. https://doi.org/10.1007/s11214-014-0057-3

Russell, C. T., & McPherron, R. L. (1973). The magnetotail and substorms. *Space Science Reviews*, *15*, 205–266.

Speiser, T. W. (1965). Particle trajectories in model current sheets: 1. Analytical solutions. *Journal of Geophysical Research*, *70*(17), 4219–4226. https://doi.org/10.1029/JZ070i017p04219

Stawarz, J. E., Ergun, R. E., & Goodrich, K. A. (2015). Generation of high-frequency electric field activity by turbulence in the Earth's magnetotail. *Journal of Geophysical Research: Space Physics*, *120*, 1845–1866. https://doi.org/10.1002/2014JA020166

Stawarz, J. E., Eriksson, S., Wilder, F. D., Ergun, R. E., Schwartz, S. J., Pouquet, A., et al. (2016). Observations of turbulence in a Kelvin-Helmholtz event on 8 September 2015 by the Magnetospheric Multiscale mission. *Journal of Geophysical Research: Space Physics*, *121*, 11,021–11,034. https://doi.org/10.1002/2016JA023458

TenBarge, J. M., & Howes, G. G. (2013). Current sheets and collisionless damping in kinetic plasma turbulence. *Astrophysical Journal Letters*, *771*(2), L27. https://doi.org/10.1088/2041-8205/771/2/L27

Torbert, R. B., Russell, C. T., Magnes, W., Ergun, R. E., Lindqvist, P. A., LeContel, O., et al. (2016). The FIELDS instrument suite on MMS: Scientific objectives, measurements, and data products. *Space Science Reviews*, *199*(1-4), 105–135. https://doi.org/10.1007/s11214-014-0109-8

Vörös, Z., Baumjohann, W., Nakamura, R., Volwerk, M., & Runov, A. (2006). Bursty bulk flow driven turbulence in the Earth's plasma sheet. *Space Science Reviews*, *122*(1–4), 301–311. https://doi.org/10.1007/s11214-006-6987-7

Wan, M., Matthaeus, W. H., Karimabadi, H., Roytershteyn, V., Shay, M., Wu, P., et al. (2012). Intermittent dissipation at kinetic scales in collisionless plasma turbulence. *Physical Review Letters*, *109*(19), 195001. https://doi.org/10.1103/PhysRevLett.109.195001

Wan, M., Matthaeus, W. H., Roytershteyn, V., Parashar, T. N., Wu, P., & Karimabadi, H. (2016). Intermittency, coherent structures and dissipation in plasma turbulence. *Physics of Plasmas*, *23*(4), 042307. https://doi.org/10.1063/1.4945631

Wan, M., Matthaeus, W. H., Servidio, S., & Oughton, S. (2013). Generation of X-points and secondary islands in 2D magnetohydrodynamic turbulence. *Physics of Plasmas*, *20*(4), 042307. https://doi.org/10.1063/1.4802985

Weygand, J. M., Kivelson, M. G., Khurana, K. K., Schwarzl, H. K., Thompson, S. M., McPherron, R. L., et al. (2005). Plasma sheet turbulence observed by Cluster II. *Journal of Geophysical Research*, *110*, A01205. https://doi.org/10.1029/2004JA010581

Yang, Y., Matthaeus, W. H., Parashar, T. N., Haggerty, C. C., Roytershteyn, V., Daughton, W., et al. (2017). Energy transfer, pressure tensor, and heating of kinetic plasma. *Physics of Plasmas*, *24*(7), 072306. https://doi.org/10.1063/1.4990421

Zimbardo, A., Greco, A., Sorriso-Valvo, L., Perri, S., Vörös, Z., Aburjania, G., et al. (2010). Magnetic turbulence in the geospace environment. *Space Science Reviews*, *156*(1-4), 89–134. https://doi.org/10.1007/s11214-010-9692-5